Parameter Calibration to Improve the Prediction of Tropical Cyclones over the Bay of Bengal Using Machine Learning–Based Multiobjective Optimization

HARISH BAKI,[a] SANDEEP CHINTA,[a] C. BALAJI,[a,b,c] AND BALAJI SRINIVASAN[a,d]

[a] *Department of Mechanical Engineering, Indian Institute of Technology Madras, Chennai, India*
[b] *Center of Excellence in Atmospheric and Climate Sciences, Indian Institute of Technology Madras, Chennai, India*
[c] *Divecha Centre for Climate Change, Indian Institute of Science, Bangalore, India*
[d] *Robert Bosch Centre for Data Science and AI, Indian Institute of Technology Madras, Chennai, India*

(Manuscript received 8 September 2021, in final form 23 February 2022)

ABSTRACT: The prediction skill of a numerical model can be enhanced by calibrating the sensitive parameters that significantly influence the model forecast. The objective of the present study is to improve the prediction of surface wind speed and precipitation by calibrating the Weather Research and Forecasting (WRF) Model parameters for the simulations of tropical cyclones over the Bay of Bengal region. Ten tropical cyclones across different intensity categories between 2011 and 2017 are selected for the calibration experiments. Eight sensitive model parameters are calibrated by minimizing the prediction error corresponding to 10-m wind speed and precipitation, using a multiobjective adaptive surrogate model-based optimization (MO-ASMO) framework. The 10-m wind speed and precipitation simulated by the default and calibrated parameter values across different aspects are compared. The results show that the calibrated parameters improved the prediction of 10-m wind speed by 17.62% and precipitation by 8.20% compared to the default parameters. The effect of calibrated parameters on other model output variables, such as cyclone track and intensities, and 500-hPa wind fields, is investigated. Eight tropical cyclones across different categories between 2011 and 2018 are selected to corroborate the performance of the calibrated parameter values for other cyclone events. The robustness of the calibrated parameters across different boundary conditions and grid resolutions is also examined. These results will have significant implications for improving the predictability of tropical cyclone characteristics, which allows us to better plan adaptation and mitigation strategies and thus help in reducing the adverse effects of tropical cyclones on society.

KEYWORDS: Tropical cyclones; Model evaluation/performance; Numerical weather prediction/forecasting; Machine learning

1. Introduction

Tropical cyclones (TCs; see the appendix for a list of acronyms) are considered among the most devastating weather phenomena in tropical regions. The frequency of occurrence of severe cyclones in the Bay of Bengal (BoB) region is found to increase at an alarming rate of 20% per hundred years, and a twofold increase has been observed during the intense cyclonic period of a year, that is, May, October, and November (Singh et al. 2000). A future projection of present global warming conditions shows that the intensity of the postmonsoon tropical cyclones over the BoB region will be much higher in the future compared to the present (Reddy et al. 2021). Densely crowded coastal cities in India adjacent to the BoB, such as Chennai, Visakhapatnam, Bhubaneswar, and Kolkata, to name a few, have been affected, in the past, by the widespread destruction caused by the tropical cyclones. An accurate prediction of the cyclone track and intensity during their landfall is inevitable to mitigate the destruction.

With the advancement achieved in measurements and computational resources, a vast amount of historical data has been generated in the past few decades. The recorded data can be used as prior information for the future forecasting of weather events. Several researchers (Estévez et al. 2020; Ghaderpour et al. 2021; Domínguez-Navarro et al. 2021) have utilized machine learning algorithms in combination with wavelet transformation to forecast daily and monthly precipitation, wind, and temperatures provided with the past historical data. The researchers reported remarkable accuracy in the short-term and long-term forecasts. However, they lack the physics information of atmospheric processes, and here the numerical weather prediction models have proven to be the best alternative.

The Weather Research and Forecasting (WRF) Model is an atmospheric simulation system, which has been used by many scientists (Osuri et al. 2013; Carroll-Smith et al. 2021) for research and operational purpose to monitor and predict the tropical cyclones across the globe. Similar to any other numerical model, the WRF Model also suffers uncertainties that arise from the specification of initial and lateral boundary conditions, representation of model physics, and the specification of the model parameters (Di et al. 2015). Many researchers (Subramani et al. 2014; Chandrasekar and Balaji 2016; Gogoi et al. 2022) have used data assimilation to improve the initial and lateral boundary conditions for the prediction of tropical cyclones over the BoB region. Several studies have been carried in the direction of parameterization schemes sensitivity—as, for example, Mukhopadhyay et al. (2011), Pattanayak et al. (2012), Osuri et al. (2012), Chandrasekar and Balaji (2012), Sandeep et al. (2018), Mohan et al. (2019), and Baki et al. (2021a)—to study the role of physics schemes

Supplemental information related to this paper is available at the Journals Online website: https://doi.org/10.1175/JAMC-D-21-0184.s1.

Corresponding author: C. Balaji, balaji@iitm.ac.in

DOI: 10.1175/JAMC-D-21-0184.1

in accurately representing the model physics and their impact on the track, intensity, and rainfall prediction of tropical cyclones over the BoB region. However, very little research has been done on parameter optimization to improve the prediction of tropical cyclones over the BoB region in the WRF Model.

Parameter calibration is a process of adjusting the model parameters to match the model output to the observations. In recent years, several researchers (Yang et al. 2012; Wang et al. 2014; Yang et al. 2015; Gong et al. 2016; Duan et al. 2017; Di et al. 2018, 2019, 2020; Chinta and Balaji 2020) have attempted to calibrate the WRF Model parameters to improve the model performance and recommended a two-step approach to be followed for the parameter calibration. They recommended that a sensitivity analysis be conducted to screen the most influential parameters. The WRF Model consists of hundreds of tunable parameters and calibrating all of them requires tremendous computational power. In addition, calibrating the parameters that show no influence on the fundamental meteorological variables may lead no improvement in the model accuracy. Thus, there is a need to identify the most sensitive parameters that greatly influence the fundamental meteorological variables. Several researchers have evaluated the sensitivity of the WRF Model parameters using qualitative and quantitative methods (Wang et al. 2013; Green and Zhang 2014; Quan et al. 2016; Di et al. 2017; Houle et al. 2017; Ji et al. 2018; Wang et al. 2020; Chinta et al. 2021; Baki et al. 2022a).

Once the sensitive parameters are estimated, the second step is to calibrate these parameters with respect to the fundamental meteorological variables. Yang et al. (2012) calibrated five parameters of the Kain–Fritsch cumulus schemes of the WRF Model using multiple very fast simulated annealing (MVFSA) (Jackson et al. 2008) algorithm and reported that the precipitation bias is reduced by a considerable amount. The authors also applied a similar methodology to calibrate five parameters of the Kain–Fritsch cumulus scheme for the predictions of East Asian summer monsoon and reported an improvement in precipitation and surface energy features with the calibrated parameters (Yang et al. 2015). Wang et al. (2014) developed the adaptive surrogate modeling-based optimization (ASMO) method that has been used by multiple researchers to calibrate the model parameters. Gong et al. (2015, 2016) extended the ASMO method for the optimization of multiple objective functions as multiobjective–adaptive surrogate modeling-based optimization (MO-ASMO) and calibrated the parameters of the land surface model. Duan et al. (2017) adopted the ASMO method to calibrate the WRF Model parameters to improve the prediction of summer monsoon over the Greater Beijing Area. With a promise found using the ASMO method, Di et al. (2018, 2019, 2020) conducted a series of studies to calibrate the WRF Model parameters across different weather phenomena over various parts of China to improve the prediction of different meteorological variables. Chinta and Balaji (2020) adopted the MO-ASMO method to calibrate the WRF Model parameters and reported that an improvement is observed for the prediction of precipitation, surface air pressure, surface air temperature, and wind speed at 10 m, during the Indian summer monsoon (ISM).

However, the optimal parameters that are obtained from a calibration study will vary with the output variable, the type of simulation event, and the geographical location (Di et al. 2020). A review of the pertinent literature shows that very little research has been done on the WRF Model parameter calibration to improve the prediction of tropical cyclones over the BoB region. In view of this, the present study focuses on improving the prediction of tropical cyclones across different intensity categories by employing parameter calibration. The model parameters utilized in the present study are obtained based on a previous investigation conducted by Baki et al. (2022a), where three different sensitivity analysis methods, namely, Morris one-at-a-time (MOAT), multivariate adaptive regression splines (MARS), and Gaussian process regression (GPR)-based Sobol' were applied to screen the most influential parameters for the simulations of tropical cyclones over the BoB region. The selected parameters are tuned in this study by minimizing the error between the model simulations and the observations of precipitation and 10-m wind speed for the simulations of 10 tropical cyclones by employing the MO-ASMO method. The performance of the calibrated parameter values is evaluated by simulating another eight tropical cyclones over the same region. In addition, an assessment of the robustness of the calibrated parameters across different spatial resolutions and driving data is also performed.

This paper is organized as follows. Section 2 describes the methodology of MO-ASMO that is adopted in the present study. Section 3 presents the WRF Model configuration, selected parameters, simulation events, data, and calibration setup. Section 4 lists the significant results obtained from the calibration and validation experiments. Conclusions from this study are presented in section 5.

2. MO-ASMO method

In comparison with standard parameter optimization approaches, the MO-ASMO technique is particularly well suited for parameter optimization of large, complicated dynamic models such as the WRF Model with high computing demands. Because the MO-ASMO technique relies mostly on the statistical surrogate model rather than the real physical model to find the ideal model solution (typically the least error between simulation and observation), the optimization convergence speed will be substantially enhanced. A flowchart of the MO-ASMO method is presented in Fig. 1.

The MO-ASMO process consists of five steps: 1) obtaining initial sampling of the physical model, 2) construction of surrogate models for each variable using the initial samples, 3) generation of new adaptive samples based on optimization of the individual surrogate models, 4) generating new adaptive samples based on multiobjective optimization, and 5) obtaining final optimized parameter values using multiple-criteria decision analysis. The following are detailed explanations of these stages.

1) A robust surrogate model requires a substantial amount of input and target data from real model simulations. As a result, the real model is simulated a sufficient number of times with various parameter values within their defined

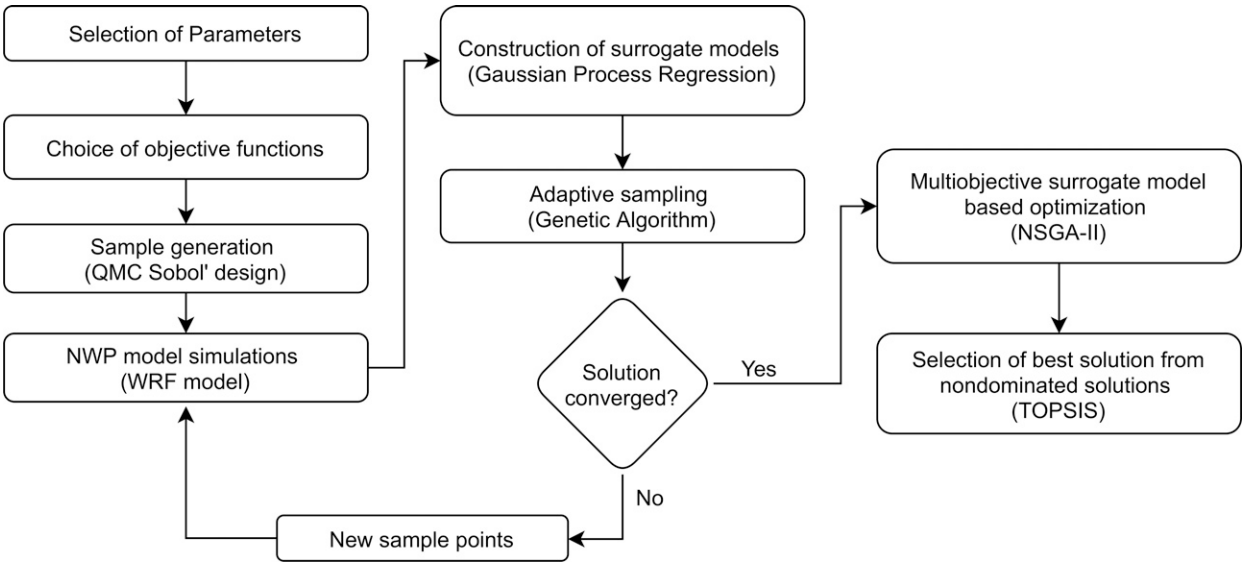

FIG. 1. Flowchart of the MO-ASMO method.

ranges. An appropriate sampling approach is used to obtain the sets of parameter values needed to run the real model, which will consistently distribute the samples throughout the parameter space. In the present study, the quasi–Monte Carlo (QMC) (Sobol' 1967) sampling design is used for parameter sampling because of its capacity to traverse the whole parameter space with relatively lean sampling points and have been used by many researchers for this purpose (Di et al. 2018, 2020). The initial parameter sample sets are generated using the QMC sampling design. The numerical simulations of the actual model are performed with these parameter values. Following this, the simulation errors are computed by comparing the model simulations with the observations. This way, the initial samples of the physical model are obtained, which consists of the parameter values as inputs and their accompanying simulations errors as the targets.

2) Construct surrogate models for individual model output variables using the initial samples to represent the actual physical model. The surrogate models are constructed using statistical regression approaches. For example, GPR, support vector machine (SVM), MARS, artificial neural network (ANN), and the sum of trees (SOT) are a few of the regression methods available. The GPR has been used by many researchers (Chinta and Balaji 2020; Di et al. 2018) and has been found to be efficient compared to other regression methods, and in view of this, it has been employed to construct the surrogate models in the present study.
3) Upon constructing the GPR surrogate models, a rapid optimization method is utilized to optimize the hyperparameters of the surrogate models. The shuffled complex evolution (Duan et al. 1993) and the genetic algorithm (GA) (Schmitt 2001), to name a few, are some of the rapid optimization algorithms available. The GA is an adaptive heuristic exploration method that uses knowledge from the previous iteration to intelligently exploit random search and lead the exploration toward the optimum solution field, which has been used in this study. With the newly obtained parameter values using the GA, the original physical model is run, and the model simulation errors are evaluated. These parameter values and simulation errors are given as new data point to the surrogate models to improve their accuracy. This way, the GPR models continue to modify as the new data points are generated. This process is called adaptive sampling, which is continued till a predefined convergence criterion for the parameter optimization is met.
4) Once optimized surrogate models for the individual variables are constructed, multiobjective optimization is performed to obtain final optimized parameters, which minimize the model simulation errors of all the variables at once. For this purpose, the nondominated sorting genetic algorithm II (NSGA-II) developed by Deb et al. (2002) is employed in this study. The NSGA-II reaches the defined objective in six steps: (i) population initialization, (ii) nondominated sorting of the population, (iii) assigning the crowding distance values to the fronts, (iv) selection of individuals, (v) genetic operator to generate new offspring, and (vi) combining new offspring and the current generation. The NSGA-II algorithm generates a Pareto front with optimum solutions called nondominated solutions. A nondominated solution is one that achieves a good balance between all goals without degrading any of them. Similar to the previous adaptive sampling, 25% of the solutions from the Pareto front that have the highest crowding distance values are chosen for the numerical simulations using the actual model, and the simulations errors are evaluated. The surrogate models are updated with the newly generated samples. This stage is continued until it reaches convergence, which is when the number of simulations of the physical model hits a predefined value.

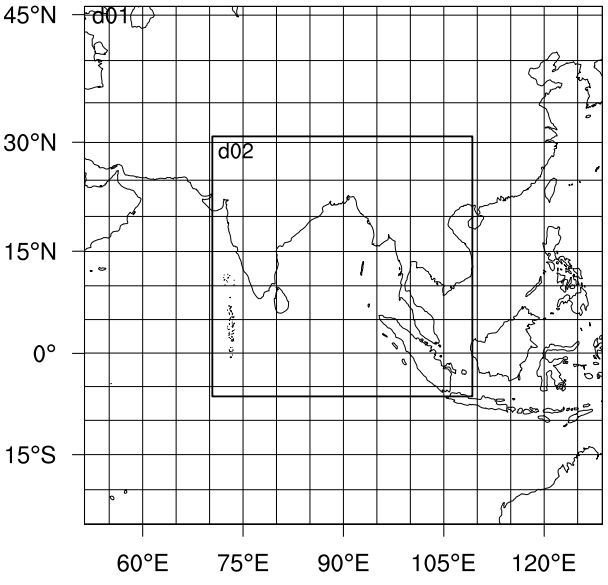

FIG. 2. An illustration of the WRF Model domain configuration. The parent domain (d01) consists of 240 × 240 grid points with 36-km resolution, and the nested domain (d02) consists of 360 × 360 grid points with 12-km resolution.

5) NSGA-II produces a final Pareto front that frequently comprises hundreds of solutions and selecting one final optimal solution out of these requires a multicriteria decision analysis. For this purpose, the technique for order of preference by similarity to ideal solution (TOPSIS) is adopted in this study. The individual variable objectives are multiplied by equal weights and are used to find the positive and negative ideal solutions. The final optimal solution has the shortest distance from the positive ideal solution and the longest distance from the negative ideal solution.

3. Design of numerical experiments

a. *WRF Model configuration and parameters selected for calibration*

The WRF Model, version 3.9.1 (Skamarock et al. 2008), is used for parameter calibration to improve the model prediction of tropical cyclones over the BoB. The two domains considered in this study are illustrated in Fig. 2. The inner domain (d02) covers the entire BoB and the adjacent Indian coastal regions. The parent domain (d01) consists of 240 × 240 grid points with a spatial resolution of 36 km, and the inner domain (d02) consists of 360 × 360 grid points with a spatial resolution of 12 km. The domain is vertically divided into terrain-following coordinates of 50 sigma layers with a fine resolution below the boundary layer. The resolution gradually becomes coarse and reaches a height of 50 hPa. The initial and boundary conditions for the simulations are taken from the National Centers for Environmental Predictions (NCEP) final (FNL) operational global analysis and forecast data at 1° × 1° resolution with a six-hourly interval (NOAA/NCEP 2000). The model domains d01 and d02 are integrated with time steps of 90 and 30 s, respectively.

The WRF Model represents the unresolved physical processes through seven parameterization schemes: surface-layer physics, land surface physics, shortwave radiation, longwave radiation, planetary boundary layer physics, microphysics, and cumulus physics. The parameterization schemes used in the present work are selected based on the studies of Baki et al. 2022a), which are MM5 similarity scheme (Beljaars 1995) for surface-layer physics, Unified Noah land surface model (Mukul Tewari et al. 2004) for land surface physics, Dudhia shortwave scheme (Dudhia 1989) for shortwave radiation, rapid radiative transfer model (Mlawer et al. 1997) for longwave radiation, WRF single-moment 6-class (WSM6) scheme (Hong and Lim 2006) for microphysics, Kain–Fritsch (Kain 2004) for cumulus physics, and Yonsei University Scheme (YSU) (Hong et al. 2006) for planetary boundary layer physics. The parameterization schemes contain a vast number of tunable parameters, and calibrating all of them is an impossible task. Baki et al. (2022a) conducted a sensitivity study of 24 parameters from the same physics schemes for tropical cyclones over the BoB and reported that a total of eight parameters were found to be most sensitive. Thus, these parameters are selected for calibration to improve the prediction of tropical cyclones over the BoB. The selected parameters and their corresponding ranges are listed in Table 1.

b. *Simulation events and data*

In this study, 18 tropical cyclones that formed in the BoB between 2011 and 2017 were chosen for the numerical experiments. The cyclones chosen are from different intensity categories that are categorized by the India Meteorological Department (IMD) according to the maximum sustained

TABLE 1. List of the sensitive parameters from seven physics schemes of the WRF Model.

Physics option	Parameter	Default	Range	Description
Surface layer	znt_zf	1	[0.5–2]	Scaling related to surface roughness
	karman	0.4	[0.35–0.42]	Von Kármán constant
Cumulus	pe	1	[0.5–2]	The multiplier for entrainment mass flux rate
Microphysics	ice_stokes_fac	14 900	[8000–30 000]	Scaling factor applied to ice fall velocity (s^{-1})
Shortwave radiation	cssca_fac	1.00×10^{-5}	[5×10^{-6}–2×10^{-5}]	Scattering tuning parameter ($m^2\ kg^{-1}$)
Longwave	secang	1.66	[1.55–1.75]	Diffusivity angle for cloud optical depth computation
Land surface	porsl	1	[0.5–2]	The multiplier for the saturated soil water content
Planetary boundary layer	pfac	2	[1–3]	Profile shape exponent for calculating the momentum diffusivity coef

TABLE 2. Overview of the tropical cyclones selected for the calibration and validation experiments.

Index	Cyclone	Intensity	Landfall time	Simulation duration
Calibration events				
A	Thane	VSCS	0100–0200 UTC 30 Dec 2011	1800 UTC 26–1800 UTC 30 Dec 2011
B	Phailin	VSCS	1700 UTC 12 Oct 2013	0600 UTC 9–0600 UTC 13 Oct 2013
C	Leher	VSCS	0830 UTC 28 Nov 2013	0000 UTC 25–0000 UTC 29 Nov 2013
D	Madi	VSCS	1700 UTC 12 Dec 2013	0600 UTC 9–0600 UTC 13 Dec 2013
E	Helen	SCS	0800–0900 UTC 22 Nov 2013	0000 UTC 19–0000 UTC 23 Nov 2013
F	Mora	SCS	0400–0500 UTC 30 May 2017	1800 UTC 26–1800 UTC 30 May 2017
G	Nilam	CS	1030–1100 UTC 31 Oct 2012	0000 UTC 28 Oct–0000 UTC 2 Nov 2012
H	Viyaru	CS	0230 UTC 16 May 2013	1800 UTC 12–1800 UTC 16 May 2013
I	Komen	CS	1400–1500 UTC 30 Jul 2015	0600 UTC 27–0600 UTC 31 Jul 2015
J	Roanu	CS	1000 UTC 21 May 2016	0000 UTC 18–0000 UTC 22 May 2016
Validation events				
K	Hudhud	VSCS	0630 UTC 12 Oct 2014	1200 UTC 8–1200 UTC 12 Oct 2014
L	Vardah	VSCS	0930–1030 UTC 12 Dec 2016	0900 UTC 9–0000 UTC 13 Dec 2016
M	Titli	VSCS	0000 UTC 11 Oct 2018	1200 UTC 7–1200 UTC 11 Oct 2018
N	Gaja	VSCS	1900–2000 UTC 15 Nov 2018	1200 UTC 12–1200 UTC 16 Nov 2018
O	Phethai	SCS	1400–1500 UTC 17 Dec 2018	0600 UTC 14–0600 UTC 18 Dec 2018
P	Nada	CS	2230–2330 UTC 1 Dec 2016	1200 UTC 28 Nov–1200 UTC 2 Dec 2016
Q	Maarutha	CS	1800–1900 UTC 16 Apr 2017	1200 UTC 13–1200 UTC 17 Apr 2017
R	Daye	CS	1900–2000 UTC 20 Sep 2018	1200 UTC 17–1200 UTC 21 Sep 2018

surface wind speed (MSW). The tropical cyclone categories used in this study are very severe cyclonic storm (64–119 kt; 1 kt $\approx$ 0.51 m s^{-1}), severe cyclonic storm (48–63 kt), and cyclonic storm (34–47 kt) (Srikanth et al. 2012). A total of 18 tropical cyclones are chosen for this study, and their details such as category, landfall time, and simulation duration are listed in Table 2, and the corresponding IMD observed tracks are illustrated in Fig. 3. Ten events are selected from the 18 cyclones for the optimization experiments to obtain the parameters that minimize the model simulation errors. These events are termed as calibration events hereinafter. The remaining eight events are selected to validate the obtained optimized parameter values. These events are termed validation events hereinafter. The cyclones are simulated for 96 h, including 12 h of spinup period, 72 h before landfall, and 12 h following landfall.

The calibration of parameters is conducted to minimize the simulation errors of wind speed at 10 m above the ground (10-m wind speed) and the total precipitation of all the events. The model simulated 10-m wind speed data are compared with the Indian Monsoon Data Assimilation and Analysis (IMDAA) data (Ashrit et al. 2020), which is available at 0.12° × 0.12° resolution, and the model simulated precipitation data is compared with the Integrated Multi-satellite Retrievals for GPM (IMERG) dataset (Huffman and Savtchenko 2019), which is available at 0.1° × 0.1° resolution. In addition to these datasets, the IMD observations of central sea level pressure (CSLP), MSW, and cyclone track are also used to evaluate the model simulations. The WRF Model variables are stored at 6-h intervals. In view of this, the observations are also taken at this latency for comparison.

c. Experimental setup for parameter calibration

In this study, the MO-ASMO method (Chinta and Balaji 2020) is used to optimize the eight sensitive parameters of the WRF Model with respect to the surface wind speed and precipitation simulations. The MO-ASMO is achieved in five steps. First, the initial parameter sets are acquired by sampling the parameters according to their ranges and distributions. Studies of Di et al. (2018, 2020) suggest that the QMC sampling method is suitable to produce uniform samples at higher dimensions. Thus, the QMC Sobol' sampling design (Sobol' 1967), which is developed in Uncertainty Quantification Python Laboratory (UQ-PyL) (Wang et al. 2016) is employed to generate the initial parameter samples sets. Di et al. (2018) stated that 10 times the dimensionality of the parameters is sufficient for the initial samples. Hence, 100 sample sets of eight parameters are generated using the QMC Sobol' sampling design. With the obtained parameter sample sets, the WRF Model simulations are performed for the calibration events that are listed in Table 2 and illustrated in Fig. 3a. The WRF Model simulations of 10-m wind speed and precipitation are compared with the observations to calculate the root-mean-square error (RMSE) (Willmott and Matsuura 2005) of each variable:

$$\mathrm{RMSE} = \sqrt{\frac{\left[\sum_{n=1}^{N}\sum_{t=1}^{T}\sum_{i=1}^{I}(\mathrm{sim}_{it}^{n} - \mathrm{obs}_{it}^{n})^2\right]}{ITN}}, \qquad (1)$$

where sim is the simulated quantity, obs is the observed quantity, I is the total number of horizontal grid points in the d02 domain, T is the dimension of simulation duration at 6-h interval, and N is the total number of calibration events. In addition to these simulations with 100 parameter sample sets, the WRF simulations with default parameters are also conducted and the corresponding RMSE values are evaluated. A normalized RMSE value (NRMSE) (Shcherbakov et al. 2013) for each of the 100 initial samples is evaluated by dividing by the default RMSE value:

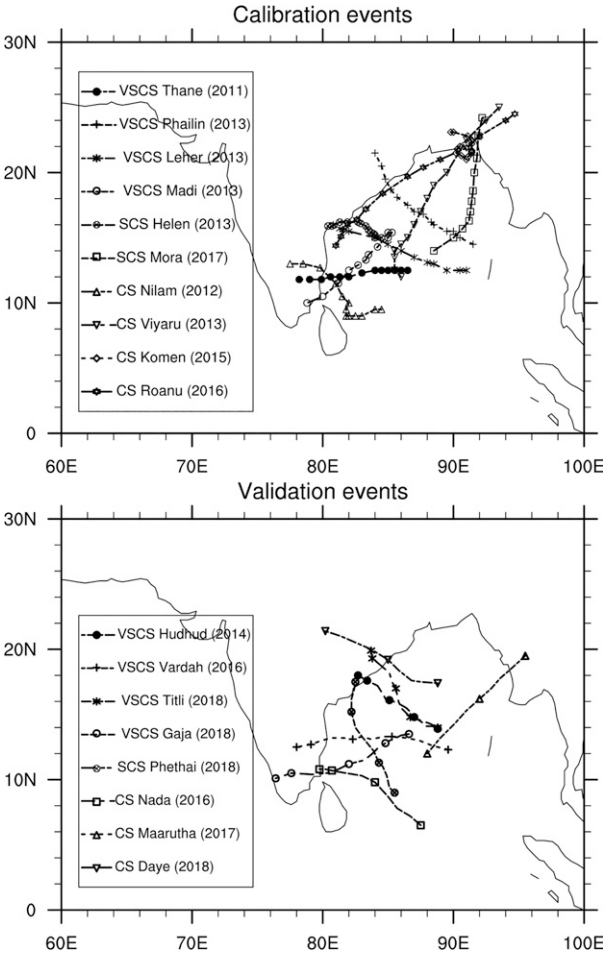

FIG. 3. An illustration of the IMD observed tracks of tropical cyclones selected for the (top) calibration and (bottom) validation experiments.

$$\mathrm{NRMSE}_i = \frac{\mathrm{RMSE}_i}{\mathrm{RMSE}_{\mathrm{def}}}, \tag{2}$$

where RMSE_i is the RMSE value of the particular parameter sample and $\mathrm{RMSE}_{\mathrm{def}}$ is the default RMSE value. Last, two datasets of 100×8 containing 100 samples sets with 8 parameter values as inputs and corresponding outputs of 100×2 containing 100 NRMSE values of 10-m wind speed and precipitation are obtained. Second, using these input and output datasets, two GPR surrogate models are constructed for each variable. Therefore, the GPR model of 10-m wind speed takes eight inputs of parameter values and one output of 10-m wind speed NRMSE value. Similarly, the GPR model of precipitation takes the same inputs but one output of precipitation NRMSE value.

The third step following the construction of the surrogate models using the initial samples is the use of the genetic algorithm to determine the optimal parameter values. With these new parameter values, the WRF Model simulations are performed, and corresponding NRMSE values are evaluated. These new parameter values and corresponding NRMSE values are added to the initial dataset, and the existing surrogate models are updated. This process of adaptive parameter sampling and updating of the surrogate models is repeated until the convergence criteria for parameter optimization is met. When the NRMSE value does not decrease continuously for 10 iterations, convergence is declared. The parameter values obtained after the convergence of each surrogate model can be considered as the optimized parameters for that particular variable. This way, one set of optimized parameter values are obtained for (i) 10-m wind speed and (ii) precipitation. However, the primary goal of the current study is to calibrate the WRF Model parameter values to minimize the NRMSE values of 10-m wind speed and precipitation simulations together. Thus, multiobjective optimization is performed with the help of NSGA-II in the fourth step.

The NSGA-II algorithm, developed in python language by Blank and Deb (2020) is utilized in the present study. The updated surrogate models of 10-m wind speed and precipitation and the ranges of parameter values are provided to the NSGA-II algorithm. The algorithm searches for optimized values with a population of 80 for 200 generations and outputs a 80×8 matrix of final optimized values. Of these 80 solutions, 20 (25% of 80) solutions with the highest crowding distances are selected for the numerical simulations, and the simulation errors along with the input parameters are used to update the existing surrogate models. This process is repeated five times, which results in 100 (20×5) model simulations, which reaches the limit for the targeted number of model runs (Chinta and Balaji 2020). The final output consists of nondominated solutions on the Pareto front, from which the best solution is identified with the application of TOPSIS multidecision criteria in the final step.

The NRMSE value is used to evaluate the accuracy of the WRF Model simulations, with NRMSE < 1 implying a better simulation relative to the default, and the parameter values with the least NRMSE value are said to be the optimal parameter values. Taylor statistics presented on a Taylor diagram (Taylor 2001) is another metric used to assess the accuracy of the model simulations. The Taylor statistics consists of a correlation coefficient, centered pattern RMS error, and normalized standard deviation. These statistics can be plotted on a single Taylor diagram, which is very helpful to explain the differences between the performances of multiple models and multiple variables. Apart from the NRMSE and Taylor statistics, another quantitative metric used to evaluate the performance of the default and calibrated parameters for the simulations precipitation is structure S, amplitude A, and location L (SAL) indices proposed by Wernli et al. (2008). The precipitation fields are segregated into objects based on the thresholds, and the S, A, and L values are evaluated. A precipitation forecast with S, A, and L values close to zero signifies a higher accuracy of that simulation.

4. Results and discussion

a. *Parameter calibration results*

1) CONVERGENCE OF SINGLE AND MULTIOBJECTIVE OPTIMIZATION RUNS

Figure 4 presents the convergence trends of the parameter optimization loops for the two quantities of interest, namely,

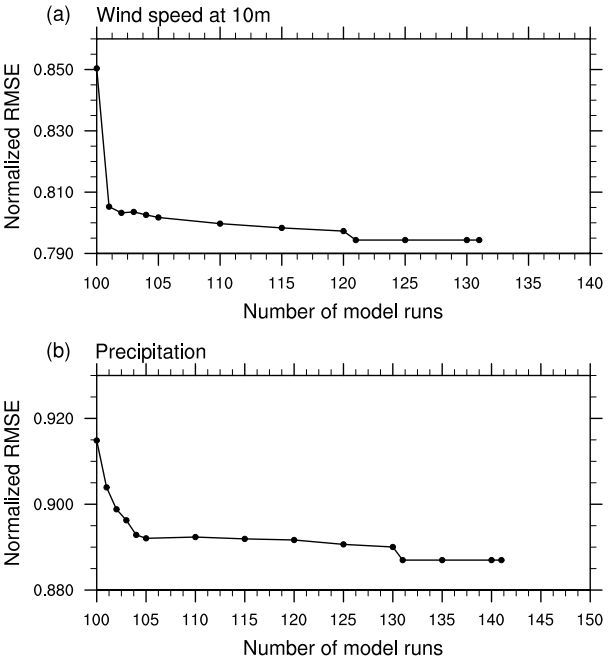

FIG. 4. Convergence trends of the surrogate models for the optimization of (a) 10-m wind speed and (b) precipitation.

(i) 10-m wind speed and (ii) precipitation, during the 84-h simulations averaged across 10 calibration events. The minimum NRMSE values from the initial 100 samples are found to be 0.850 for the 10-m wind speed and 0.915 for the precipitation, which implies that the simulation errors are decreased by 15% (10-m wind speed) and 9.05% (precipitation) using the initial 100 samples themselves when compared with the default parameters. The additional numbers of model runs required for the convergence of 10-m wind speed and precipitation optimization are 21 and 31, respectively. The parameter values obtained at these iterations are termed as the corresponding variable optimized parameters. Beyond these runs, no reduction in the NRMSE is observed for the next 10 iterations. The minimum NRMSE values found at the converged iterations are listed in Table 3 and show that the simulation errors are reduced by 20.56% (10-m wind speed) and 11.30% (precipitation). Because the present study aims to improve the prediction of 10-m wind speed and precipitation together, the NSGA-II optimization is employed to perform multiobjective optimization. The NSGA-II produces a Pareto front of nondominated solutions after five iterations as shown in Fig. 5, in which the abscissa indicates the NRMSE values of 10-m wind speed and the ordinate indicates the NRMSE values of the precipitation. The NRMSE values of 10-m wind speed range from 0.79 to 0.99, and that of the precipitation range from 0.89 to 0.96. The Pareto front clearly shows that the least NRMSE value of 10-m wind speed has the highest NRMSE value of precipitation, which indicates that improving one variable will degrade another variable. Thus, the TOPSIS method with a weight of 0.5 to each of the two objectives is employed to obtain the final best solution, which is

TABLE 3. Final NRMSE values obtained from the optimization of 10-m wind speed, precipitation, and the combination (multiobjective) of 10-m wind speed and precipitation. The values shown in boldface text indicate the NRMSE reduction achieved from the single objective optimization of the corresponding variables.

Optimization runs	10-m wind speed	Precipitation
10-m wind speed optimization	**0.7944**	0.9637
Precipitation optimization	1.1853	**0.8870**
Multiobjective optimization	0.8239	0.9180

marked as the black star in Fig. 5. Hereinafter, the parameter values in the best solution are considered as the calibrated parameter values. A total of 252 (100 + 21 + 31 + 100) WRF Model runs were required to obtain the final calibrated parameter values. The final NRMSE values after the calibration, as shown in Table 3, reveal that a considerable deviation is observed from the single objective optimized NRMSE values. This can be explained by Fig. 5, which shows that improving one variable will lead to the degradation in another variable. Also, the simulation errors after the calibration are reduced by 17.62% (10-m wind speed) and 8.20% (precipitation).

2) COMPARISON OF RMSE VALUES FOR THE WRF SIMULATIONS WITH DEFAULT AND OPTIMIZED PARAMETERS

Figure 6 presents the RMSE values of 10-m wind speed simulated with the optimized parameters of 10-m wind speed and precipitation simulated with the optimized parameters of precipitation, in comparison with the default parameter simulations, for the 10 calibration events A–J. The results clearly show a significant reduction in the simulation RMSE values by the optimized parameters compared to the default parameters. The reduction in errors with the predictions of 10-m wind speed is the highest for event E (30.68%) and the lowest

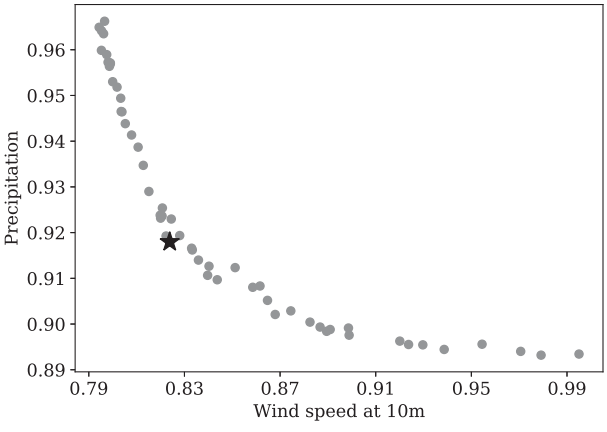

FIG. 5. Pareto front of the nondominated solutions obtained from the NSGA-II multiobjective optimization, with the black star indicating the final solution obtained by applying the TOPSIS method. The values on the abscissa and ordinate indicate the NRMSE values of wind speed at 10-m height and precipitation, respectively.

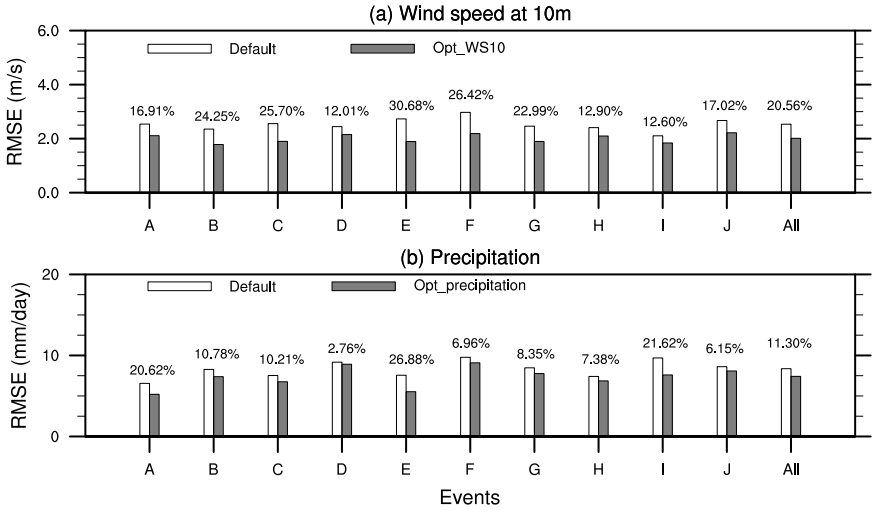

FIG. 6. RMSE values of the (a) 10-m wind speed simulations using the parameters obtained from the 10-m wind speed optimization and (b) precipitation simulations using the parameters obtained from the precipitation optimization, in comparison with the default RMSE values, for the calibration events (labels A–J). The percentage values indicate the reduction in the RMSE value of variables when using the optimized parameters relative to the default parameters.

for event D (12.01%). As stated earlier, the improvement in 10-m wind speed for all the events combined together is 20.56%. Similarly, the precipitation simulation RMSE reduction ranges from 2.76% for event D to 26.88% for event E, and the combined reduction is 11.30% for all the events together. The results show that the individual optimization of 10-m wind speed or precipitation can significantly improve the respective variable simulations. The parameters obtained from the individual optimizations can be adopted in any study to improve the respective outcomes of numerical simulations of tropical cyclones over the BoB region, that is, when only that particular variable is of interest to us.

Figure 7 shows a comparison of RMSE values of the calibrated simulations with the default simulations for the 10 calibration events A–J over the BoB region, which indicates a general trend of reduction in the RMSE. The reduction in the errors with the simulations of the 10-m wind speed ranges from 7.84% for event D to 26.30% for event E, and the reduction is 17.62% for all the events combined. Similarly, the RMSE in precipitation reduced from 2.99% for event D to

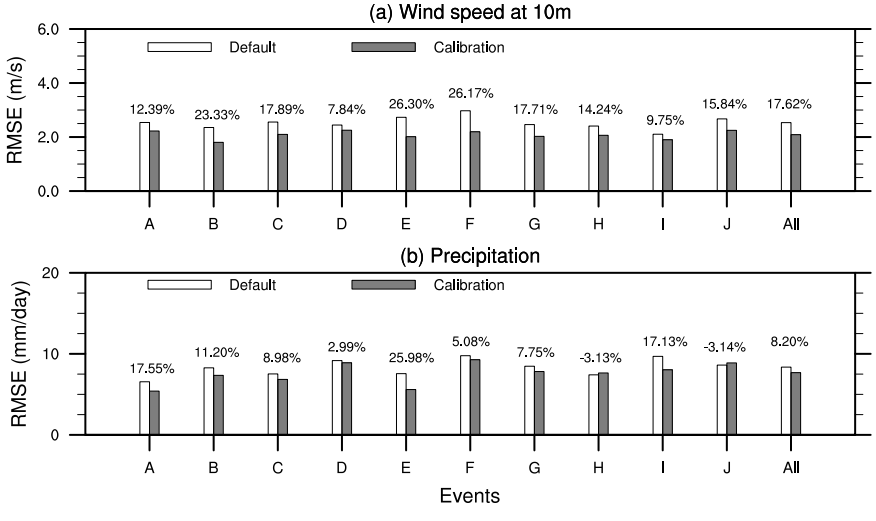

FIG. 7. RMSE values of the (a) 10-m wind speed (b) precipitation simulations using the calibrated parameters that are obtained from the multiobjective optimization of 10-m wind speed and precipitation simultaneously, in comparison with the default RMSE values, for the calibration events A–J.

25.98% for event E, and the reduction is 8.20% for all the events combined. However, some events show a marginal increase in RMSE value (−3.13% for event H and −3.14% for event J) for the precipitation simulation, which can be attributed to the definition of optimization objective function that focuses on the cumulative NRMSE value of all the events together rather than individual events. Thus, a few events with a small increase in the errors are unavoidable. However, there is a very good overall improvement is seen. These results show that the calibrated parameters can improve the simulations of 10-m wind speed and precipitation together and are consistent over the 10 calibration events. In addition to the comparison of individual events, the time evolution of RMSE values for the WRF simulations with default and calibrated parameters at different lead times are also compared and shown in Fig. S1 in the online supplemental material. The results clearly show that the calibrated parameters improved the WRF simulations of 10-m wind speed and precipitation at a 6-hourly lead time over the default simulations. The improvement in 10-m wind speed simulations ranges from 10.09% to 21.03%, and the improvement in precipitation simulations ranges from 3.02% to 14.58%.

3) Comparison of spatial distributions for the WRF simulations with default and calibrated parameters

Spatial distributions of the domain averaged 10-m wind speed and precipitation for the 10 calibration events together simulated with the default and calibration parameters are presented in Figs. S2 and S3, respectively, in the online supplemental material. The IMDAA dataset is used as the ground truth for 10-m wind speed, and the IMERG rainfall data are used for precipitation. Figures S2a–c show that the 10-m wind speed simulated with the default set of parameters and calibrated set of parameters have similar intensities and spatial coverage. However, the simulations from both default and calibrated parameters underestimate the intensities when compared with the observations. Figures S2d and S2e show that the default simulations have huge spatial coverage of ± 1 m s^{-1} bias over the land, 2 m s^{-1} positive bias over the BoB region, and 3 m s^{-1} positive bias over the central BoB region. In addition, the default simulations show a positive bias of more than 4 m s^{-1} over a small portion of the east coast region. In contrast, the calibrated simulations show ± 1 m s^{-1} bias over a major portion of the domain, except over the central BoB region, over which a positive bias of 2 m s^{-1} is seen. The spatial plots indicate that the calibrated parameters simulate the 10-m wind speed better than the default parameters over the ocean and coastal regions, which are the most affected areas during the occurrence of a cyclone.

The spatial distributions of observed and simulated precipitation are presented in Figs. S3a–c in the online supplemental material. The simulations with the default and calibrated set of parameters underestimated the precipitation in terms of intensity and spatial coverage when compared with the observations. However, the calibrated parameters simulated the precipitation with better spatial coverage and intensity than the simulations from the default parameters. Figures S3d and S3e show that the significant differences between the default and calibrated simulations are seen over the Bangladesh coast, northern BoB, central BoB, and southeast BoB region. The default simulations show larger 8 mm day^{-1} positive bias structures over the Bangladesh coast, which is higher compared to the calibrated simulations. The calibrated simulation shows broad structures of 4 mm day^{-1} positive bias over the central BoB, whereas the default simulations show narrow structures of 8 mm day^{-1} positive bias. The default simulations show large 4 mm day^{-1} positive bias structures over the southeast BoB and Sri Lanka coast, whereas the calibrated simulations show similar structures with lesser bias. In contrast, both the simulations show similar spatial coverage of 8 mm day^{-1} negative bias over the northern BoB region. These results indicate that the calibrated parameters simulated the precipitation better than the default parameters.

4) Comparison of Taylor statistics and SAL indices for the WRF simulations with default and calibrated parameters

The spatial plots show a visual comparison that provides qualitative differences between the default and calibrated simulations. The Taylor statistics and the SAL indices are evaluated to examine the differences quantitatively and are shown in Fig. 8. The Taylor statistics are calculated for the 10-m wind speed and precipitation, whereas the SAL indices are calculated only for the precipitation as suggested by the studies of Wernli et al. (2008). Figure 8a shows that the calibrated 10-m wind speed simulations have less bias, less centered RMSE, and similar variations to that of observations when compared to the default simulations. However, both the simulations have the same correlation coefficient. The calibrated precipitation simulations show a smaller bias, less centered RMSE, and a higher correlation coefficient when compared to the default simulations. The default precipitation simulations have normalized standard deviation close to the observed one, whereas the calibrated simulations have smaller variations when compared to the observations. These results show that the calibrated 10-m wind speed and precipitation simulations are positioned close to the reference compared to the default simulations, which indicates that the 10-m wind speed and the precipitation are better simulated with the calibrated parameter values compared to the default.

The structure S, amplitude A, and location L scores of the precipitation simulated with default and calibrated parameters are presented in Fig. 8b. The structure value of calibrated precipitation (0.0522) is closer to zero when compared with the default precipitation (0.1003), which indicates that the precipitation objects of calibrated simulations are larger and have lesser variations than the observations. In contrast, the default precipitation objects are smaller in size with similar variations to that of the observations. The structure scores imply that the calibrated simulations captured the size and shape of precipitation objects better than the default simulations. The amplitude score of calibrated precipitation (0.0365) is

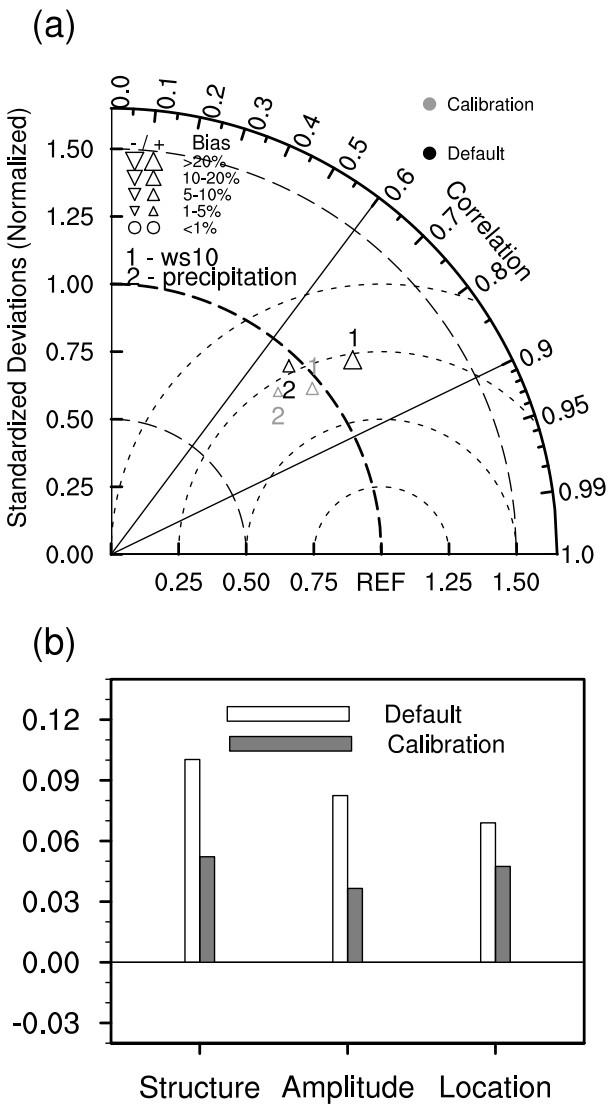

FIG. 8. Comparison of (a) Taylor statistics of 10-m wind speed and precipitation and (b) SAL indices of precipitation for the simulations of calibration events A–J with default and calibrated parameter values.

closer to zero when compared with the default precipitation (0.0825), indicating that the calibrated simulations have a smaller bias than the default simulations and have captured the intensity better. Since the objective function of optimization is designed to improve the RMS error between the simulations and observations, the amplitude score reflects the optimization by improving bias and intensity. The location score of calibrated precipitation (0.0474) is also closer to zero when compared with the default precipitation (0.069), which indicates that the calibrated parameters simulate the precipitation with a smaller spatial deviation relative to the default parameters. These results further corroborate the superior performance of calibrated parameters over the default for the precipitation simulations.

5) IMPACT OF CALIBRATED PARAMETERS ON CYCLONE TRACK AND INTENSITY

The impact of calibrated parameters on the simulations of cyclone track and intensity is examined by comparing the RMSE values between the IMD observations and the WRF simulations with default and calibrated parameters for the 10 calibration events A–J as shown in Fig. S4 in the online supplemental material. The relative improvement of the calibrated simulations over the default simulations is also shown above the RMSE bars. The results clearly show that the calibrated parameters improve the simulations of cyclone track, CSLP, and MSW over the default parameters with an overall improvement of 12.62%, 6.93%, and 4.86%, respectively. The reduction in RMSE of cyclone track ranges from 1.78% for event G to 51.46% for event C; however, the simulations of calibrated parameters for the events E, H, and I show an increased RMSE, which is unavoidable since the goal here is an overall reduction in RMSE across all the events. The reduction in RMSE of CSLP ranges from 2.41% for event A to 59.27% for event F, and the events E, I, and J show an increased RMSE. Similarly, the reduction in RMSE of MSW ranges from 0.36% for event H to 40.85% for event H, while event D alone shows an increased RMSE. These results imply that the calibrated parameters better capture the cyclone track, CSLP, and MSW over the default parameters.

A comparison of the evolution of CSLP and MSW for each event has also been conducted and shown in Fig. 9. The results show that the WRF simulations with default and calibrated parameters have captured the intensity evolution but have underestimated the cyclone intensity in terms of CSLP and MSW. The CSLP simulations of default and calibrated parameters show a relatively similar order of intensity for all the events except for F, for which the default parameters overestimated the intensity with a deviation of 50 hPa, whereas the calibrated parameters overestimated the intensity with a deviation of 10 hPa. For the MSW simulations, the calibrated parameters show a little better performance than the default parameters for every event, except for D, for which the calibrated simulations show a deviation of 20 m s^{-1}, whereas the default simulations show a deviation of 10 m s^{-1}. These results suggest that the overall performance of calibrated parameters is relatively better than the default parameters.

6) IMPACT OF CALIBRATED PARAMETERS ON THE ATMOSPHERIC STRUCTURE

The objective function of the calibration method is designed to minimize the deviation between observations and simulations of wind speed and precipitation at the surface level. However, the calibration of surface-level fields will have an impact on the upper-atmospheric variables positively or negatively. The impact of calibration on the higher-level atmospheric structure is therefore examined by observing the velocity field at 500 hPa for event 3 (Cyclone Leher) and event 6 (Cyclone Mora). Figure 10 show the 500-hPa velocity field of Cyclone Leher at the end of the first, second, and third days, simulated by the default and calibrated parameters and

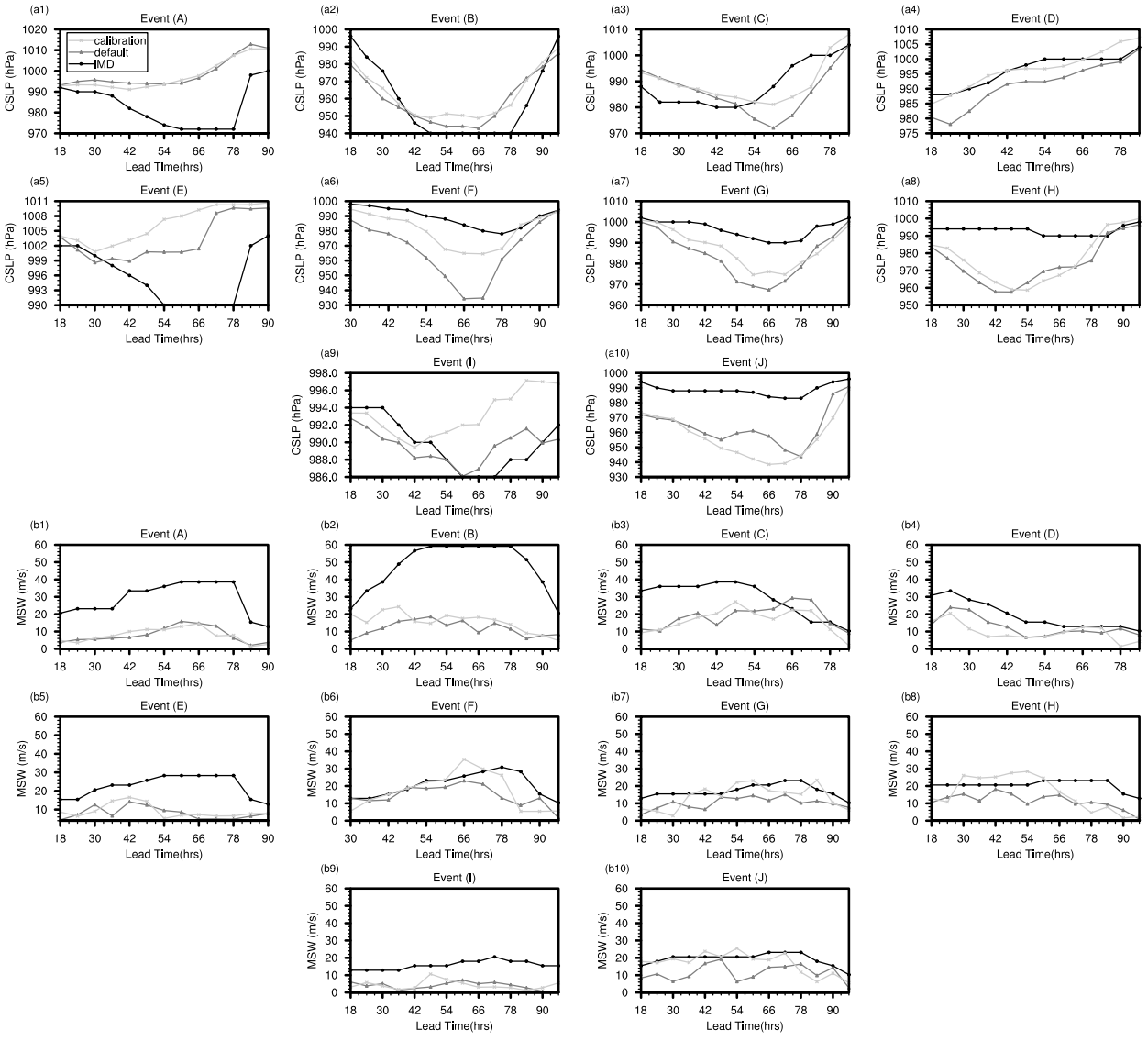

FIG. 9. Comparisons of the time evolution simulations of (a1)–(a10) CSLP and (b1)–(b10) MSW, for the calibration events A–J, using the default and calibration parameters, in comparison with the IMD observations.

compared with the observations. The observed velocity fields clearly show a cyclonic circulation at the end of all days and an anticyclonic circulation at the end of the second and third days. The default parameters simulated a cyclonic circulation at the end of the first and second days with an overestimated intensity relative to the observations and an anticyclonic circulation at the end of all days. However, the locations of cyclonic and anticyclonic circulations have deviated from the observations, and the structure of the anticyclonic circulation is also different from the observations. The calibrated parameters simulated a cyclonic circulation at the end of all days with a relatively similar intensity to observations and an anticyclonic circulation at the end of all days with a similar structure to that of observations. The cyclonic and anticyclonic circulations are also very close to the observations as compared with the default simulations. Similarly, Fig. 11 shows a comparison of 500-hPa velocity field between the observations and simulations with default and calibrated parameters, for Cyclone Mora, at the end of the first, second, and third days. The observations clearly show a cyclonic circulation at the end of the first, second, and third days. The default parameters simulated a cyclonic circulation at the end of the first and second days with an overestimation relative to the observations. However, there is no circulation simulated at the end of the third day. The calibrated parameters simulated a cyclonic circulation at the end of all days with lesser intensity than the default parameters. Although the locations of the cyclonic circulation at the end of the first and second simulated by the default and calibrated parameters are very close to the observations, the intensity of the circulation simulated

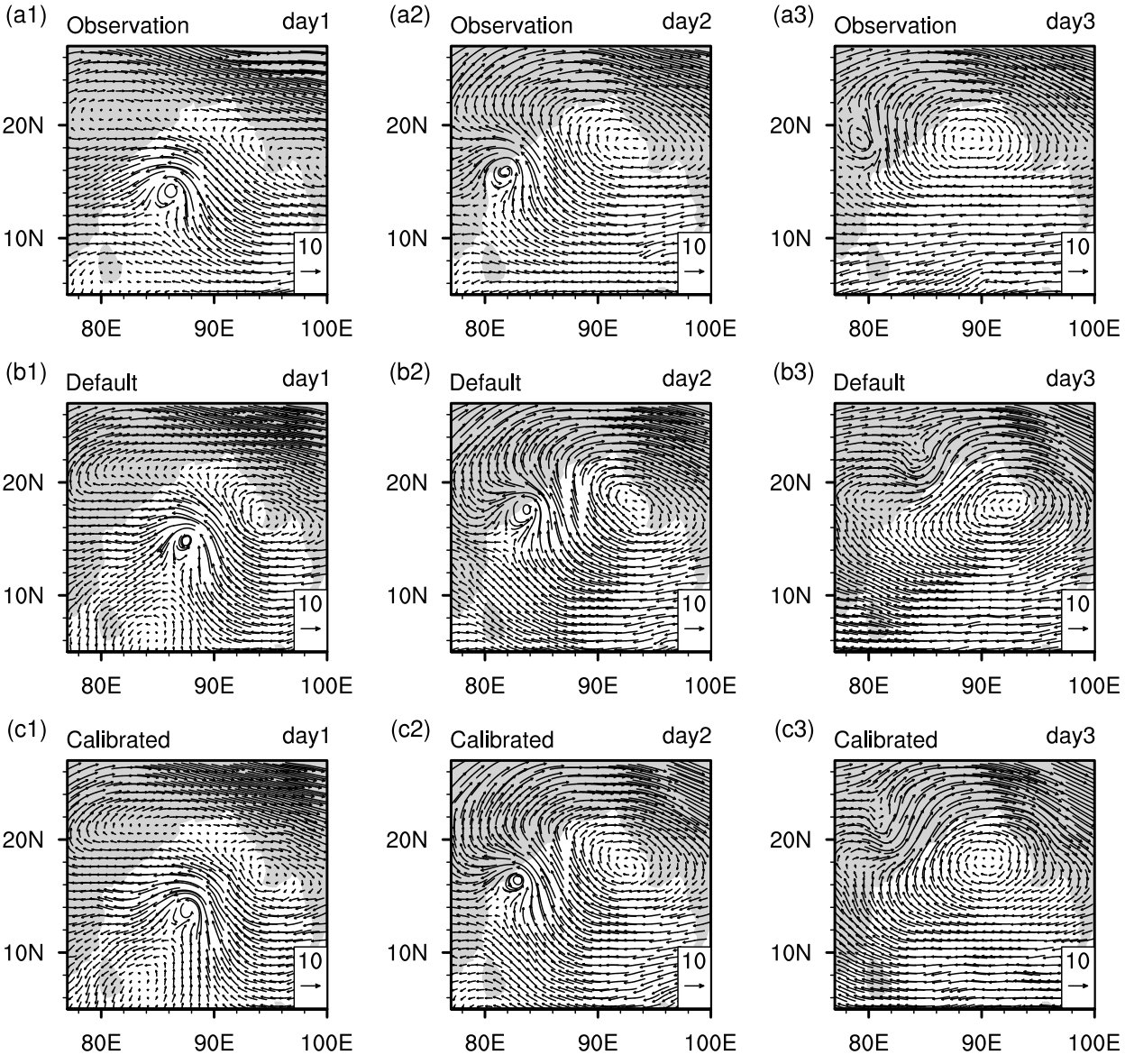

FIG. 10. An illustration of the wind velocity field at 500 hPa for the simulation of VSSC Leher, showing (a1)–(a3) observations at the end of day 1, day 2, and day 3; (b1)–(b3) the simulations with default parameters; and (c1)–(c3) the simulations with calibrated parameters. Reference to the magnitude of the velocity field is given in the bottom-right box in each plot; the length of the displayed vector indicates a magnitude of 10 m s^{-1}.

by the calibrated parameters simulated is better than the default parameters. These results indicate that the calibration indeed improves the 500-hPa-level atmospheric structure.

b. *Verifying the robustness of the calibrated parameters for other events*

To corroborate the robustness of the calibrated parameters, eight new tropical cyclone events, which are different from the calibration events and are referred to as the validation events hereinafter are simulated using the WRF Model. The details of the validation events are presented in Table 2 and the corresponding IMD observed tracks are shown in Fig. 3b. The validation events are also simulated using the same configuration as the calibration experiments, including domain configuration, simulation duration, physics schemes, and boundary data.

Figure 12 shows a comparison of RMSE values of the WRF simulations with the calibrated and the default parameters for the eight validation events K–R over the BoB region, which indicate a general trend of reduction in the RMSE. The reduction in the error of 10-m wind speed in terms of the RMSE ranges from 3.54% for event P to 21.12% for event K, and the reduction in the overall RMSE is 13.30%. Similarly, the RMSE reduction for precipitation ranges from 4.12% for

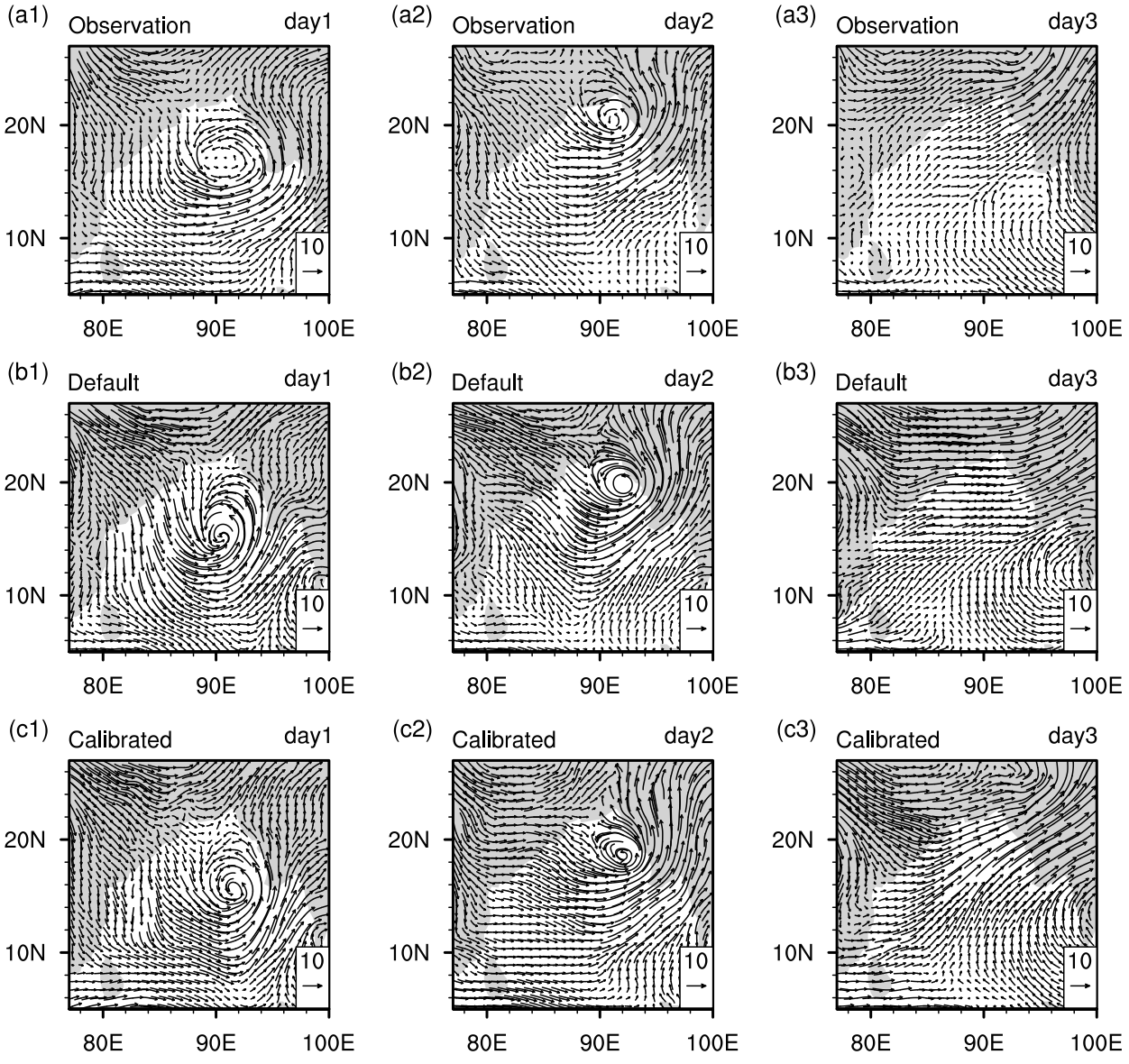

FIG. 11. As in Fig. 10, but for the simulation of SCS Mora.

event K to 13.66% for event O, and the overall reduction is 5.36% for all the events considered together. It is apparent that the calibrated parameters improved the simulations of calibration events as well as the validation events. Similar to the calibration events, the time evolution of wind speed and precipitation (figures not shown) simulated by the calibrated parameters show an improving trend over the default parameters for the validation events.

Spatial plots of the domain averaged 10-m wind speed and precipitation simulations (figures not shown) indicate that the calibrated parameters simulated the variables close to observations with less bias than the default simulations. The Taylor statistics are evaluated for the validation events to examine further the quantitative differences between the default and calibrated simulations and are presented in Fig. 13. The Taylor statistics of 10-m wind speed show that the calibrated simulations have lesser bias and RMS errors than the default simulations and a standard deviation similar to that of the observed one. In contrast, the default 10-m wind speed simulations have a smaller correlation coefficient than the calibrated simulations and a standard deviation higher than that of the observed one. Similarly, the Taylor statistics of precipitation show that the calibrated simulations have lesser RMS error and higher correlation coefficient than the default simulations, a standard deviation close to that of the observed one, and a bias similar to that of default simulations. The Taylor statistics of 10-m wind speed and precipitation simulated by the calibrated parameters are positioned close to the reference than the default simulations, indicating the better performance of the calibrated parameters.

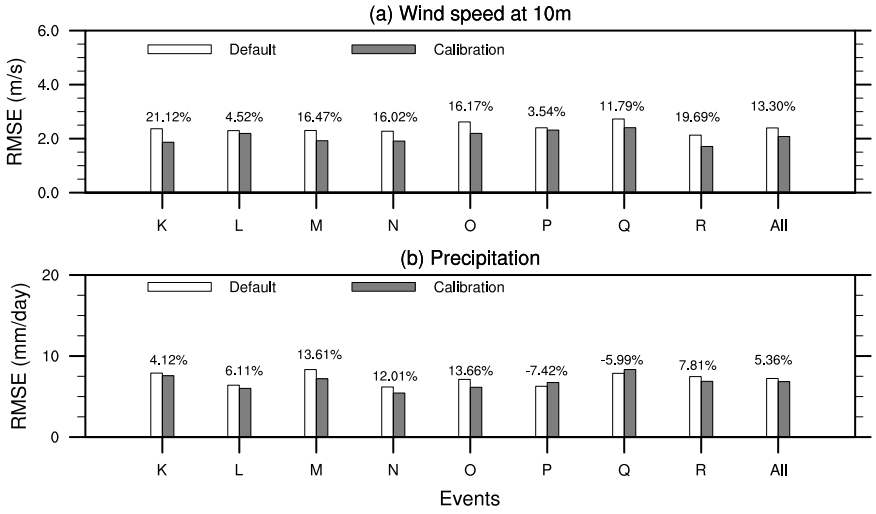

FIG. 12. Comparison of the RMSE values of (a) 10-m wind speed and (b) precipitation, simulated using the WRF Model with default and calibrated parameters, for the validation events K–R.

c. *Impact of calibrated parameters on simulations with different boundary conditions*

To examine the robustness of the calibrated parameters across different boundary conditions, the fifth major global reanalysis produced by ECMWF (ERA5) data with a 1.0° grid is used to drive the WRF simulations of the calibration and validation events A–R. The simulation experiments adopted the configurations that of the calibration experiments, such as model configuration, simulation area, and simulation duration, except for the boundary conditions, for which the ERA5 data are used. The performance of the calibrated parameters is evaluated by comparing the RMSE values of 10-m wind speed and precipitation.

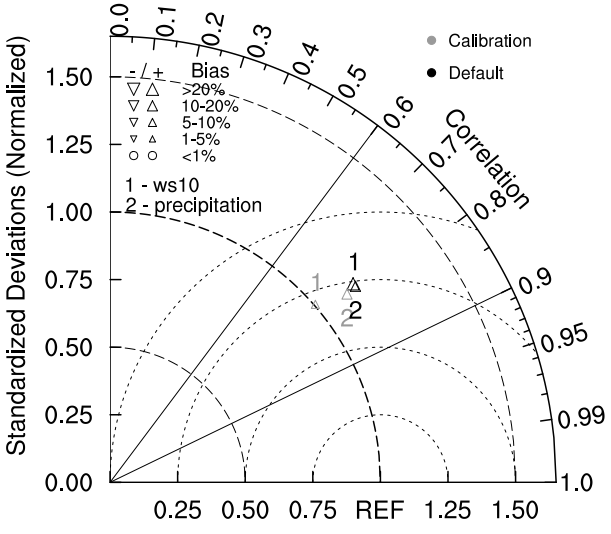

FIG. 13. Comparison of Taylor statistics of 10-m wind speed and precipitation for the simulations of validation events K–R using the default and calibrated parameter values.

Figure S5 in the online supplemental material presents the RMSE values of 10-m wind speed and precipitation simulations with default and calibration parameters, for the total events A–R, by considering the ERA5 data as the boundary conditions. The results clearly show a better performance of the calibrated parameter values over the default ones by reducing the RMSE values. The reduction in the RMSE of the 10-m wind speed ranges from 4.80% for event D to 24.52% for event F, and the overall reduction is 13.01% for all the events considered together. Similarly, the RMSE reduction for precipitation ranges from 0.14% for event J to 21.32% for event E, and the overall reduction is 6.57% for all the events considered together. Although the events Q and O show an increase in RMSE of 1.62% and 6.24% for the 10-m wind speed and precipitation simulations, respectively, the overall reduction compensated for this increment. From these results, it can be concluded that the calibrated parameter values still simulate better forecasts of 10-m wind speed and precipitation compared to the default parameter values for the simulations of tropical cyclones over the BoB region even if the boundary conditions are replaced from FNL to ERA5.

d. *Impact of calibrated parameters on simulations with different grid resolutions*

To investigate the robustness of the calibrated parameters for the simulations of tropical cyclones over the BoB region at different spatial resolutions, two sets of WRF simulations with grid resolutions different from the calibration experiments are conducted to simulate the observed events A–R. The experiments include single-domain simulations with a 12-km grid resolution and nested-domain simulations with a 12-km outer-domain resolution and a 4-km inner-domain grid resolution. The number of grid points in the outer domain (d01) is 520 × 520, and the inner domain (d02) is 960 × 960. The WRF Model domain configuration of these two

TABLE 4. Final parameter values obtained from the optimization of 10-m wind speed, precipitation, and the calibrated parameters.

Parameter	Default	Opt_ws10	Opt_rain	Calibration
znt_zf	1	2	0.5293	2
karman	0.4	0.42	0.3503	0.4
pe	1	0.5001	0.5123	0.5001
ice_stokes_fac	14 900	29 999.7672	28 500.5724	29 915.6267
cssca (cssca_fac)	1.00×10^{-5}	5.00×10^{-6}	1.99×10^{-5}	5.00×10^{-6}
secang	1.66	1.7474	0.5019	0.5041
porsl	1	0.5	1.8594	0.5011
pfac	2	3	2.9893	2.9999

experiments is illustrated in Fig. S6 in the online supplemental material. These simulations differ from the calibration simulations. The change in grid resolution leads to a change in the number of grid points to maintain the simulation area similar to that of the calibration experiments. Since the parent domain grid resolution is at 12 km, the driving boundary conditions taken at 0.25° grid is a best practice. However, there are no FNL data at 0.25° available before the 2014 period, which is required for the simulations of the selected tropical cyclones. Thus, the ERA5 data with a 0.25° grid are used to drive the WRF simulations for both experiments. The remaining configurations, including physics schemes and simulation duration, are similar to that of the calibration and validation simulations. The performance of the calibrated parameters is evaluated by comparing the RMSE values of 10-m wind speed and precipitation.

Figure S7 in the online supplemental material presents a comparison of RMSE values of 10-m wind speed and precipitation simulations with default and calibration parameter values on a 12-km single domain for the observed simulation events A–R. The calibration parameters have better 10-m wind speed and precipitation simulation capabilities than those with the default parameters. The reduction in the RMSE of the 10-m wind speed ranges from 4.38% for event Q to 23.91% for event F, and the overall reduction is 12.56% for all the events considered together. Similarly, the RMSE for precipitation reduces from 2.13% for event C to 17.05% for event M, and the overall reduction is 7.93% for all the events considered together. The 10-m wind speed simulations show that calibrated parameters decreased the RMSE values for all the events. However, the overall improvement is a little less than the calibration and validation experiments together (15.79%). Similarly, the precipitation simulations show that the calibrated parameters decreased the RMSE values for all the events except event O, and the overall improvement is even higher than the calibration and validation experiments together (which is 7.13%). These results suggest that calibrated parameters can improve the 10-m wind speed and precipitation simulations on a 12-km single domain with ERA5 boundary data at 0.25° grid and demonstrate the superior performance of the calibration parameters over the default parameters.

For the 4-km-grid-resolution nested-domain experiments, Fig. S8 in the online supplemental material presents a comparison of RMSE values of 10-m wind speed and precipitation simulations with default and calibration parameter values for the observed simulation events A–R. The reduction in the RMSE of the 10-m wind speed ranges from 1.91% for event C to 24.49% for event F, and the overall reduction is 10.97% for all the events considered together. Similarly, the RMSE for precipitation reduces from 1.92% for event L to 18.60% for event M, and the overall reduction is 7.40% for all the events considered together. The 10-m wind speed simulations show that calibrated parameters decreased the RMSE values for all the events except events L and Q, and the overall improvement is far less compared to the calibration and validation experiments together (which is 15.79%). Similarly, the precipitation simulations show that the calibrated parameters decreased the RMSE values for all the events except events H, J, and O, and the overall improvement is a little higher than the calibration and validation experiments together. Although the performance of the calibrated parameters is better than the default parameters, the improvement in RMSE is lesser compared to that of calibration and validation experiments. As a whole, the performance of the calibrated parameters is superior to that of the default parameters for the simulations of tropical cyclones over the BoB region, even at 12-km single-domain simulations and 4-km nested-domain simulations.

e. *Physical interpretation of the calibrated parameter values*

The parameter values obtained from the described optimizations experiments and the default values are listed in Table 4, which indicates that the parameters have highly inconsistent variations among them. Compared with default values, the calibrated parameter values are increased for znt_zf, ice_stokes_fac, and pfac, whereas the values decreased for pe, cssca_fac, secang, and porsl, and the value of Karman is unchanged. It is impractical to constitute a straightforward relationship between the parameters and the simulated model output variables because of the nonlinear interactions present among the various physical processes (Di et al. 2018; Chinta and Balaji 2020).

The znt_zf parameter (scaling related to surface roughness) is used in the surface-layer scheme, which directly controls the roughness length and affects the surface wind speed. A higher znt_zf value means a higher roughness length that results in decreased 10-m wind speed. The Karman parameter (von Kármán constant) is used in both surface-layer and planetary boundary layer schemes, which governs the flow speed profile in a wall-normal shear flow and influences the bulk transfer coefficient of momentum, heat, moisture, and diffusivity coefficient of momentum. A higher Karman value can increase the exchange coefficient of momentum (surface drag

coefficient) and decrease the surface wind speed. At the same time, a higher Karman value can increase the bulk transfer coefficient of moisture that leads to an increase in precipitation. The parameter Pe (multiplier for entrainment mass flux rate) is used in the cumulus physics scheme, which regulates the entraining of ambient air into the updraft air parcel. A lower Pe value indicates a smaller amount of entrainment, which makes the atmosphere more unstable and helps in the formation of deep convective clouds, which ultimately leads to heavy convective precipitation. The ice_stokes_fac (scaling factor applied to icefall velocity) is used in the microphysics scheme, which controls the terminal fall velocity of cloud ice particles. A higher ice_stokes_fac value increases the sedimentation of ice crystals and increases the conversion from cloud ice to rainwater, resulting in increased precipitation. The cssca_fac is used in the shortwave radiation scheme, which governs the attenuation of downward shortwave radiation. A smaller value of cssca_fac leads to less attenuation and scattering of solar radiation, resulting in a higher amount of solar radiation reaching Earth's surface, which increases the evaporation at the surface that causes an increase in precipitation. The parameter secang (diffusivity angle for cloud optical depth computation) is used in the longwave radiation scheme, which governs the attenuation of the longwave radiation irradiated by the clouds toward Earth's surface. Similar to the csscs_fac, a smaller value of secang results in less attenuation, increasing the amount of longwave radiation reaching Earth's surface, which ultimately results in higher precipitation. The parameter porsl (multiplier for the saturated soil water content) is used in the land surface scheme, which plays a vital role in heat exchange between land and atmosphere through moisture evapotranspiration in soil. A high value of porsl increases the evaporation of soil water, leading to an increase in precipitation. The parameter pfac (profile shape exponent for calculating the momentum diffusivity coefficient) is used in the planetary boundary layer scheme, contributing to the diffusion of turbulence eddies in the boundary layer. A higher value of pfac increases the vertical momentum diffusion and thereby increases the wind speed. In addition, a higher value of pfac also increases the heat diffusion, which makes more evaporation of water vapor from the ground and leads to higher precipitation. Because all of the parameters have a very nonlinear relationship with the model output variables, explaining the calibrated parameter values becomes quite difficult. Nevertheless, the calibrated parameters obtained in this study improved the prediction of precipitation and wind speed for the simulations of 18 tropical cyclones over the BoB region relative to the default parameter values.

5. Conclusions

The present study employed the multiobjective adoptive surrogate model-based optimization (MO-ASMO) framework to calibrate the eight sensitive parameters of the WRF Model to reduce the simulations simulation errors of 10-m wind speed and precipitation for the tropical cyclones over the Bay of Bengal region. The parameters were sampled using the quasi–Monte Carlo Sobol' design to create the initial parameter sets, using which the WRF Model simulations of the calibration events were performed. Two surrogate models of Gaussian process regression were constructed, one each for 10-m wind speed and precipitation. The surrogate models were optimized using the genetic algorithm in an iterative process. The optimized parameter values of 10-m wind speed improved the 10-m wind speed simulations by 20.56%, and that of the precipitation improved the precipitation simulations by 11.30%. After this, the NSGA-II algorithm was employed as a multiobjective optimization and a Pareto front containing a set of nondominated solutions of optimal parameters values was obtained. The final best solution is sorted by utilizing the TOPSIS method. The described calibration methodology yields three sets of optimal parameter values: one set minimizes the NRMSE values of 10-m wind speed, another set minimizes the NRMSE values of precipitation, and the calibration set minimizes the NRMSE values of 10-m wind speed and precipitation together.

The performance of the calibrated parameter values over the default values was evaluated by comparing the NRMSE values, spatial distributions, Taylor statistics, and the SAL indices for the simulations of calibration events. The results showed that the calibrated parameters improved the 10-m wind speed and precipitation simulations by 17.62% and 8.20%, respectively, and outperformed the default parameters in every other aspect. A comparison of the cyclone track and intensity simulations showed that the calibrated parameters reduced the track error by 12.62%, CSLP error by 6.93%, and MSW error by 4.86%. In addition to the surface fields, an examination of the wind velocity field at 500 hPa revealed that the simulations carried out with the calibrated parameters were close to the observations. Further, the performance of the calibrated parameter values was validated for a different set of cyclone events and found that an improvement of 13.30% and 5.36% observed for 10-m wind speed and precipitation. Finally, the robustness of the calibrated parameter values across different boundary conditions and grid resolutions was also examined by taking the boundary conditions from 1° and 0.25° ERA5 reanalysis data and conducting the WRF simulations at 12-km single-domain and 4-km nested-domain resolutions. The calibrated parameters obtained in this study were found to be robust across different precipitation events, driving data, and domain resolutions.

Although the present work improves the predictability of tropical cyclone precipitation and wind speeds, these two are not the only important variables for cyclones, which limits the applicability of this method for certain cases. There are some other variables, such as surface pressure, relative humidity, and surface temperature, whose contribution toward the formation and intensification of tropical cyclones is considerably high. Thus, future studies can be conducted to improve the variables based on their importance. Improving the initial conditions provided to the calibrated model by assimilating the observation data could further help in improving the model predictions (Baki et al. 2022b).

Acknowledgments. The model simulations are performed on the Aqua High-Performance Computing (HPC) system

at the Indian Institute of Technology Madras (IITM), Chennai, India, and the Aaditya HPC system at the Indian Institute of Tropical Meteorology (IITM), Pune, India. The authors thank the "Centre of Excellence (CoE) in climate change impact on coastal infrastructure and the adaptation strategies" for their suggestions. The Ministry of Human Resource and Development is funding research Grant 11/9/209-U.3(A) for this project (SB20210835CEMHRD008502) under the Atmospheric and Climate Sciences Laboratory. The authors declare that there are no conflicts of interest to disclose.

Data availability statement. The WRF Model main source code is modified according to the authors' requirement to enable the parameter values given as inputs through the namelist.input file. The modified source code and the namelist.input files that are used for the simulations can be downloaded from a repository (https://doi.org/10.5281/zenodo.5150524; Baki et al. 2021b). The WRF Model is built in FORTRAN 90 language. The software can be installed in any Linux-based system. The Python-language-based application programming interfaces (API) are used for the machine learning algorithms, namely, Gaussian process regression (GPR) (https://scikit-learn.org/stable/modules/generated/sklearn.gaussian_process.GaussianProcessRegressor.html#), genetic algorithm (GA) (https://github.com/rmsolgi/geneticalgorithm), and nondominated sorted genetic algorithm-II (NSGA-II) (https://pymoo.org/). These APIs are publicly available, and the contact information can be found at the respective websites.

APPENDIX

Acronyms Used in this Article

ANN	Artificial neural network
ASMO	Adaptive surrogate model-based optimization
BoB	Bay of Bengal
CS	Cyclonic storm
CSLP	Central sea level pressure
ECMWF	European Centre for Medium-Range Weather Forecasts
ERA5	Fifth major global reanalysis produced by ECMWF
FNL	Final
GA	Genetic algorithm
GPR	Gaussian process regression
IMD	India Meteorological Department
IMDAA	Indian Monsoon Data Assimilation and Analysis
IMERG	Integrated Multi-satellite Retrievals for GPM
ISM	Indian summer monsoon
MARS	Multivariate adaptive regression splines
MOAT	Morris one-at-a-time
MO-ASMO	Multiobjective adaptive surrogate model-based optimization
MSW	Maximum sustained wind speed
MVFSA	Multiple very fast simulated annealing
NCEP	National Centers for Environmental Prediction
NSGA-II	Nondominated sorting genetic algorithm II
NRMSE	Normalized root-mean-square error
QMC	Quasi–Monte Carlo
RMSE	Root-mean-square error
SAL	Structure, amplitude, and location
SCS	Severe cyclonic storm
SOT	Sum of trees
SVM	Support vector machine
TC	Tropical cyclone
TOPSIS	Technique for order of preference by similarity to ideal solution
UQ-PyL	Uncertainty quantification Python laboratory
VSCS	Very severe cyclonic storm
WRF	Weather Research and Forecasting Model
WSM6	WRF single-moment 6-class
YSU	Yonsei University scheme

REFERENCES

Ashrit, R., and Coauthors, 2020: IMDAA regional reanalysis: Performance evaluation during Indian summer monsoon season. *J. Geophys. Res. Atmos.*, **125**, e2019JD030973, https://doi.org/10.1029/2019JD030973.

Baki, H., S. Chinta, C. Balaji, and B. Srinivasan, 2021a: A sensitivity study of WRF Model microphysics and cumulus parameterization schemes for the simulations of tropical cyclones using GPM radar data. *J. Earth Syst. Sci.*, **130**, 190, https://doi.org/10.1007/s12040-021-01682-3.

——, ——, ——, and ——, 2021b: Dataset for the publication of "WRF Model parameter calibration to improve the prediction of tropical cyclones over the Bay of Bengal using machine learning-based multiobjective optimization." Zenodo, accessed 22 June 2022, https://doi.org/10.5281/zenodo.5150524.

——, ——, ——, and ——, 2022a: Determining the sensitive parameters of WRF Model for the prediction of tropical cyclones in the Bay of Bengal using global sensitivity analysis and machine learning. *Geosci. Model Dev.*, **15**, 2133–2155, https://doi.org/10.5194/gmd-15-2133-2022.

——, C. Balaji, and B. Srinivasan, 2022b: Impact of data assimilation on a calibrated WRF Model for the prediction of tropical cyclones over the Bay of Bengal. *Curr. Sci.*, **122**, 569–583, https://doi.org/10.18520/cs/v122/i5/569-583.

Beljaars, A. C., 1995: The parametrization of surface fluxes in large-scale models under free convection. *Quart. J. Roy. Meteor. Soc.*, **121**, 255–270, https://doi.org/10.1002/qj.49712152203.

Blank, J., and K. Deb, 2020: Pymoo: Multi-objective optimization in Python. *IEEE Access*, **8**, 89 497–89 509, https://doi.org/10.1109/ACCESS.2020.2990567.

Carroll-Smith, D., R. J. Trapp, and J. M. Done, 2021: Exploring inland tropical cyclone rainfall and tornadoes under future climate conditions through a case study of Hurricane Ivan. *J. Appl. Meteor. Climatol.*, **60**, 103–118, https://doi.org/10.1175/JAMC-D-20-0090.1.

Chandrasekar, R., and C. Balaji, 2012: Sensitivity of tropical cyclone Jal simulations to physics parameterizations. *J. Earth Syst. Sci.*, **121**, 923–946, https://doi.org/10.1007/s12040-012-0212-8.

——, and ——, 2016: Impact of physics parameterization and 3DVAR data assimilation on prediction of tropical cyclones

in the Bay of Bengal region. *Nat. Hazards*, **80**, 223–247, https://doi.org/10.1007/s11069-015-1966-5.

Chinta, S., and C. Balaji, 2020: Calibration of WRF model parameters using multiobjective adaptive surrogate model-based optimization to improve the prediction of the Indian summer monsoon. *Climate Dyn.*, **55**, 631–650, https://doi.org/10.1007/s00382-020-05288-1.

——, J. Yaswanth Sai, and C. Balaji, 2021: Assessment of WRF model parameter sensitivity for high-intensity precipitation events during the Indian summer monsoon. *Earth Space Sci.*, **8**, e2020EA001471, https://doi.org/10.1029/2020EA001471.

Deb, K., A. Pratap, S. Agarwal, and T. Meyarivan, 2002: A fast and elitist multiobjective genetic algorithm: NSGA-II. *IEEE Trans. Evol. Comput.*, **6**, 182–197, https://doi.org/10.1109/4235.996017.

Di, Z., and Coauthors, 2015: Assessing WRF model parameter sensitivity: A case study with 5 day summer precipitation forecasting in the Greater Beijing Area. *Geophys. Res. Lett.*, **42**, 579–587, https://doi.org/10.1002/2014GL061623.

——, Q. Duan, W. Gong, A. Ye, and C. Miao, 2017: Parametric sensitivity analysis of precipitation and temperature based on multi-uncertainty quantification methods in the Weather Research and Forecasting model. *Sci. China Earth Sci.*, **60**, 876–898, https://doi.org/10.1007/s11430-016-9021-6.

——, ——, C. Wang, A. Ye, C. Miao, and W. Gong, 2018: Assessing the applicability of WRF optimal parameters under the different precipitation simulations in the Greater Beijing Area. *Climate Dyn.*, **50**, 1927–1948, https://doi.org/10.1007/s00382-017-3729-3.

——, J. Ao, Q. Duan, J. Wang, W. Gong, C. Shen, Y. Gan, and Z. Liu, 2019: Improving WRF model turbine-height windspeed forecasting using a surrogate-based automatic optimization method. *Atmos. Res.*, **226**, 1–16, https://doi.org/10.1016/j.atmosres.2019.04.011.

——, Q. Duan, C. Shen, and Z. Xie, 2020: Improving WRF typhoon precipitation and intensity simulation using a surrogate-based automatic parameter optimization method. *Atmosphere*, **11**, 89, https://doi.org/10.3390/atmos11010089.

Domínguez-Navarro, J. A., T. B. Lopez-Garcia, and S. M. Valdivia-Bautista, 2021: Applying wavelet filters in wind forecasting methods. *Energies*, **14**, 3181, https://doi.org/10.3390/en14113181.

Duan, Q., V. K. Gupta, and S. Sorooshian, 1993: Shuffled complex evolution approach for effective and efficient global minimization. *J. Optim. Theory Appl.*, **76**, 501–521, https://doi.org/10.1007/BF00939380.

——, and Coauthors, 2017: Automatic model calibration: A new way to improve numerical weather forecasting. *Bull. Amer. Meteor. Soc.*, **98**, 959–970, https://doi.org/10.1175/BAMS-D-15-00104.1.

Dudhia, J., 1989: Numerical study of convection observed during the winter monsoon experiment using a mesoscale two-dimensional model. *J. Atmos. Sci.*, **46**, 3077–3107, https://doi.org/10.1175/1520-0469(1989)046<3077:NSOCOD>2.0.CO;2.

Estévez, J., J. A. Bellido-Jiménez, X. Liu, and A. P. Garca-Marn, 2020: Monthly precipitation forecasts using wavelet neural networks models in a semiarid environment. *Water*, **12**, 1909, https://doi.org/10.3390/w12071909.

Ghaderpour, E., T. Vujadinovic, and Q. K. Hassan, 2021: Application of the least-squares wavelet software in hydrology: Athabasca River basin. *J. Hydrol. Reg. Stud.*, **36**, 100847, https://doi.org/10.1016/j.ejrh.2021.100847.

Gogoi, R. B., G. Kutty, and A. Borgohain, 2022: Impact of INSAT-3D satellite-derived wind in 3DVAR and hybrid ensemble-3DVAR data assimilation systems in the simulation of tropical cyclones over the Bay of Bengal. *Model. Earth Syst. Environ.*, **8**, 1813–1823, https://doi.org/10.1007/s40808-021-01183-8.

Gong, W., Q. Duan, J. Li, C. Wang, Z. Di, Y. Dai, A. Ye, and C. Miao, 2015: Multi-objective parameter optimization of common land model using adaptive surrogate modelling. *Hydrol. Earth Syst. Sci.*, **19**, 2409–2425, https://doi.org/10.5194/hess-19-2409-2015.

——, ——, ——, ——, ——, A. Ye, C. Miao, and Y. Dai, 2016: Multiobjective adaptive surrogate modeling-based optimization for parameter estimation of large, complex geophysical models. *Water Resour. Res.*, **52**, 1984–2008, https://doi.org/10.1002/2015WR018230.

Green, B. W., and F. Zhang, 2014: Sensitivity of tropical cyclone simulations to parametric uncertainties in air–sea fluxes and implications for parameter estimation. *Mon. Wea. Rev.*, **142**, 2290–2308, https://doi.org/10.1175/MWR-D-13-00208.1.

Hong, S.-Y., and J.-O. J. Lim, 2006: The WRF single-moment 6-class microphysics scheme (WSM6). *Asia-Pac. J. Atmos. Sci.*, **42**, 129–151.

——, Y. Noh, and J. Dudhia, 2006: A new vertical diffusion package with an explicit treatment of entrainment processes. *Mon. Wea. Rev.*, **134**, 2318–2341, https://doi.org/10.1175/MWR3199.1.

Houle, E. S., B. Livneh, and J. R. Kasprzyk, 2017: Exploring snow model parameter sensitivity using Sobol' variance decomposition. *Environ. Modell. Software*, **89**, 144–158, https://doi.org/10.1016/j.envsoft.2016.11.024.

Huffman, G and Savtchenko, AK, 2019: GPM IMERG Final Precipitation L3 Half Hourly 0.1 degree × 0.1 degree V06. GES DISC, accessed 23 September 2020, https://doi.org/10.5067/GPM/IMERG/3B-HH/06.

Jackson, C. S., M. K. Sen, G. Huerta, Y. Deng, and K. P. Bowman, 2008: Error reduction and convergence in climate prediction. *J. Climate*, **21**, 6698–6709, https://doi.org/10.1175/2008JCLI2112.1.

Ji, D., W. Dong, T. Hong, T. Dai, Z. Zheng, S. Yang, and X. Zhu, 2018: Assessing parameter importance of the Weather Research and Forecasting model based on global sensitivity analysis methods. *J. Geophys. Res. Atmos.*, **123**, 4443–4460, https://doi.org/10.1002/2017JD027348.

Kain, J. S., 2004: The Kain–Fritsch convective parameterization: An update. *J. Appl. Meteor.*, **43**, 170–181, https://doi.org/10.1175/1520-0450(2004)043<0170:TKCPAU>2.0.CO;2.

Mlawer, E. J., S. J. Taubman, P. D. Brown, M. J. Iacono, and S. A. Clough, 1997: Radiative transfer for inhomogeneous atmospheres: RRTM, a validated correlated-*k* model for the longwave. *J. Geophys. Res.*, **102**, 16 663–16 682, https://doi.org/10.1029/97JD00237.

Mohan, P. R., C. V. Srinivas, V. Yesubabu, R. Baskaran, and B. Venkatraman, 2019: Tropical cyclone simulations over Bay of Bengal with ARW model: Sensitivity to cloud microphysics schemes. *Atmos. Res.*, **230**, 104651, https://doi.org/10.1016/j.atmosres.2019.104651.

Mukhopadhyay, P., S. Taraphdar, and B. Goswami, 2011: Influence of moist processes on track and intensity forecast of cyclones over the north Indian Ocean. *J. Geophys. Res.*, **116**, D05116, https://doi.org/10.1029/2010JD014700.

Mukul Tewari, N., and Coauthors, 2004: Implementation and verification of the unified NOAH land surface model in the WRF Model (formerly paper number 17.5). *20th Conf. on*

Weather Analysis and Forecasting/16th Conf. on Numerical Weather Prediction, Seattle, WA, Amer. Meteor. Soc., 14.2a, https://ams.confex.com/ams/pdfpapers/69061.pdf.

NOAA/NCEP, 2000: NCEP FNL Operational Model Global Tropospheric Analyses, continuing from July 1999. National Center for Atmospheric Research Computational and Information Systems Laboratory Research Data Archive, accessed 23 September 2020, https://doi.org/10.5065/D6M043C6.

Osuri, K. K., U. Mohanty, A. Routray, M. A. Kulkarni, and M. Mohapatra, 2012: Customization of WRF-ARW model with physical parameterization schemes for the simulation of tropical cyclones over north Indian Ocean. *Nat. Hazards*, **63**, 1337–1359, https://doi.org/10.1007/s11069-011-9862-0.

——, ——, ——, M. Mohapatra, and D. Niyogi, 2013: Real-time track prediction of tropical cyclones over the north Indian Ocean using the ARW model. *J. Appl. Meteor. Climatol.*, **52**, 2476–2492, https://doi.org/10.1175/JAMC-D-12-0313.1.

Pattanayak, S., U. Mohanty, and K. K. Osuri, 2012: Impact of parameterization of physical processes on simulation of track and intensity of Tropical Cyclone Nargis (2008) with WRF-NMM model. *Sci. World J.*, **2012**, 1–18, https://doi.org/10.1100/2012/671437.

Quan, J., Z. Di, Q. Duan, W. Gong, C. Wang, Y. Gan, A. Ye, and C. Miao, 2016: An evaluation of parametric sensitivities of different meteorological variables simulated by the WRF model. *Quart. J. Roy. Meteor. Soc.*, **142**, 2925–2934, https://doi.org/10.1002/qj.2885.

Reddy, P. J., D. Sriram, S. Gunthe, and C. Balaji, 2021: Impact of climate change on intense Bay of Bengal tropical cyclones of the post-monsoon season: A pseudo global warming approach. *Climate Dyn.*, **56**, 2855–2879, https://doi.org/10.1007/s00382-020-05618-3.

Sandeep, C., C. Krishnamoorthy, and C. Balaji, 2018: Impact of cloud parameterization schemes on the simulation of cyclone Vardah using the WRF model. *Curr. Sci.*, **115**, 1143–1153, https://doi.org/10.18520/cs/v115/i6/1143-1153.

Schmitt, L. M., 2001: Theory of genetic algorithms. *Theor. Comput. Sci.*, **259**, 1–61, https://doi.org/10.1016/S0304-3975(00)00406-0.

Shcherbakov, M. V., and Coauthors, 2013: A survey of forecast error measures. *World Appl. Sci. J.*, **24**, 171–176, https://doi.org/10.5829/idosi.wasj.2013.24.itmies.80032.

Singh, O., T. A. Khan, and M. S. Rahman, 2000: Changes in the frequency of tropical cyclones over the north Indian Ocean. *Meteor. Atmos. Phys.*, **75**, 11–20, https://doi.org/10.1007/s007030070011.

Skamarock, W. C., J. B. Klemp, J. Dudhia, D. O. Gill, D. M. Barker, W. Wang, and J. G. Powers, 2008: A description of the Advanced Research WRF version 3. NCAR Tech. Note NCAR/TN-475+STR, 113 pp., https://doi.org/10.5065/D68S4MVH.

Sobol', I. M., 1967: On the distribution of points in a cube and the approximate evaluation of integrals. *Zh. Vychisl. Mat. Mat. Fiz.*, **7**(4), 86–112, https://doi.org/10.1016/0041-5553(67)90144-9.

Srikanth, L., M. Ramalingam, M. S. George, L. Bertino, and A. Samuelsen, 2012: A study on the influence of oceanic and atmospheric parameters on tropical cyclones in the Bay of Bengal. *Eur. J. Sci. Res.*, **76**, 63–73.

Subramani, D., R. Chandrasekar, K. S. Ramanujam, and C. Balaji, 2014: A new ensemble-based data assimilation algorithm to improve track prediction of tropical cyclones. *Nat. Hazards*, **71**, 659–682, https://doi.org/10.1007/s11069-013-0942-1.

Taylor, K. E., 2001: Summarizing multiple aspects of model performance in a single diagram. *J. Geophys. Res.*, **106**, 7183–7192, https://doi.org/10.1029/2000JD900719.

Wang, C., Q. Duan, W. Gong, A. Ye, Z. Di, and C. Miao, 2014: An evaluation of adaptive surrogate modeling based optimization with two benchmark problems. *Environ. Modell. Software*, **60**, 167–179, https://doi.org/10.1016/j.envsoft.2014.05.026.

——, ——, C. H. Tong, Z. Di, and W. Gong, 2016: A GUI platform for uncertainty quantification of complex dynamical models. *Environ. Modell. Software*, **76**, 1–12, https://doi.org/10.1016/j.envsoft.2015.11.004.

——, and Coauthors, 2020: Assessing the sensitivity of land-atmosphere coupling strength to boundary and surface layer parameters in the WRF model over Amazon. *Atmos. Res.*, **234**, 104738, https://doi.org/10.1016/j.atmosres.2019.104738.

Wang, J., X. Li, L. Lu, and F. Fang, 2013: Parameter sensitivity analysis of crop growth models based on the extended Fourier amplitude sensitivity test method. *Environ. Modell. Software*, **48**, 171–182, https://doi.org/10.1016/j.envsoft.2013.06.007.

Wernli, H., M. Paulat, M. Hagen, and C. Frei, 2008: SAL—A novel quality measure for the verification of quantitative precipitation forecasts. *Mon. Wea. Rev.*, **136**, 4470–4487, https://doi.org/10.1175/2008MWR2415.1.

Willmott, C. J., and K. Matsuura, 2005: Advantages of the mean absolute error (MAE) over the root mean square error (RMSE) in assessing average model performance. *Climate Res.*, **30**, 79–82, https://doi.org/10.3354/cr030079.

Yang, B., Y. Qian, G. Lin, R. Leung, and Y. Zhang, 2012: Some issues in uncertainty quantification and parameter tuning: A case study of convective parameterization scheme in the WRF regional climate model. *Atmos. Chem. Phys.*, **12**, 2409–2427, https://doi.org/10.5194/acp-12-2409-2012.

——, Y. Zhang, Y. Qian, A. Huang, and H. Yan, 2015: Calibration of a convective parameterization scheme in the WRF model and its impact on the simulation of East Asian summer monsoon precipitation. *Climate Dyn.*, **44**, 1661–1684, https://doi.org/10.1007/s00382-014-2118-4.